

This manuscript has been authored by UT-Battelle, LLC under Contract No. DE-AC05-00OR22725 with the U.S. Department of Energy. The United States Government retains and the publisher, by accepting the article for publication, acknowledges that the United States Government retains a non-exclusive, paid-up, irrevocable, world-wide license to publish or reproduce the published form of this manuscript, or allow others to do so, for United States Government purposes. The Department of Energy will provide public access to these results of federally sponsored research in accordance with the DOE Public Access Plan (<http://energy.gov/downloads/doe-public-access-plan>).

Tuning Fermi Levels in Intrinsic Antiferromagnetic Topological Insulators MnBi_2Te_4 and MnBi_4Te_7 by Defect Engineering and Chemical Doping

Mao-Hua Du^{1,*}, Jiaqiang Yan¹, Valentino R. Cooper¹, and Markus Eisenbach²

¹Materials Science and Technology Division and ²Center for Computational Sciences,

Oak Ridge National Laboratory, Oak Ridge, TN 37831, USA

*mhdu@ornl.gov

Abstract

MnBi₂Te₄ and MnBi₄Te₇ are intrinsic antiferromagnetic topological insulators, offering a promising materials platform for realizing exotic topological quantum states. However, high densities of intrinsic defects in these materials not only cause bulk metallic conductivity, preventing the measurement of quantum transport in surface states, but may also affect magnetism and topological properties. In this paper, we show by density functional theory calculations that the strain induced by the internal heterostructure promotes the formation of large-size-mismatched antisite defect Bi_{Mn} in MnBi₂Te₄; such strain is further enhanced in MnBi₄Te₇, giving rise to even higher Bi_{Mn} density. The abundance of intrinsic Bi_{Mn} donors results in degenerate n-type conductivity under the Te-poor growth condition. Our calculations suggest that growths in a Te-rich condition can lower the Fermi level, which is supported by our transport measurements. We further show that the internal strain can also enable efficient doping by large-size-mismatched substitutional Na_{Mn} acceptors, which can compensate Bi_{Mn} donors and lower the Fermi level. Na doping may pin the Fermi level inside the bulk band gap even at the Te-poor limit in MnBi₂Te₄. Furthermore, facile defect formation in MnSb₂Te₄ and its implication in Sb doping in MnBi₂Te₄ as well as the defect segregation in MnBi₄Te₇ are discussed. The defect engineering and doping strategies proposed in this paper will stimulate further studies for improving synthesis and for manipulating magnetic and topological properties in MnBi₂Te₄, MnBi₄Te₇, and related compounds.

I. Introduction

Topological insulators (TI) have bulk gaps but metallic surface/edge states with linear dispersion protected by the time reversal symmetry (TRS)[1-4]. The presence of a long-range magnetic order in a TI can break the TRS and opens an exchange gap in the surface states; this could lead to a variety of exotic topological quantum states, including quantum anomalous Hall (QAH) effect and axion insulator states[1,2]. Extensive research has been carried out to search for materials platforms that enable the observation of these quantum phenomena[5-8].

MnBi_2Te_4 and related van der Waals (vdW) heterostructures $(\text{MnBi}_2\text{Te}_4)(\text{Bi}_2\text{Te}_3)_n$ have recently emerged as a new class of intrinsic antiferromagnetic (AFM) TIs.[9-18] MnBi_2Te_4 consists of stacked septuple layers (SLs) of Te-Bi-Te-Mn-Te-Bi-Te as shown in Figure 1(a). Bi_2Te_3 quintuple layers (QLs) can be inserted between MnBi_2Te_4 SLs to form $(\text{MnBi}_2\text{Te}_4)(\text{Bi}_2\text{Te}_3)_n$ [e.g., MnBi_4Te_7 ($n = 1$) and $\text{MnBi}_6\text{Te}_{10}$ ($n = 2$)] [see Figure 1(b) for the crystal structure of MnBi_4Te_7].[19] In these compounds, Mn ions have the intralayer FM coupling while the interlayer coupling is AFM, forming A-type AFM ordering.[20,21] The Dirac surface states have been demonstrated in MnBi_2Te_4 and MnBi_4Te_7 by angle-resolved photoemission spectroscopy (ARPES) and theoretical calculations.[9-15,18] The QAH effect[16] and the axion insulator state[17] have recently been reported in MnBi_2Te_4 with odd and even number of SLs, respectively, but have not yet been demonstrated in MnBi_4Te_7 .

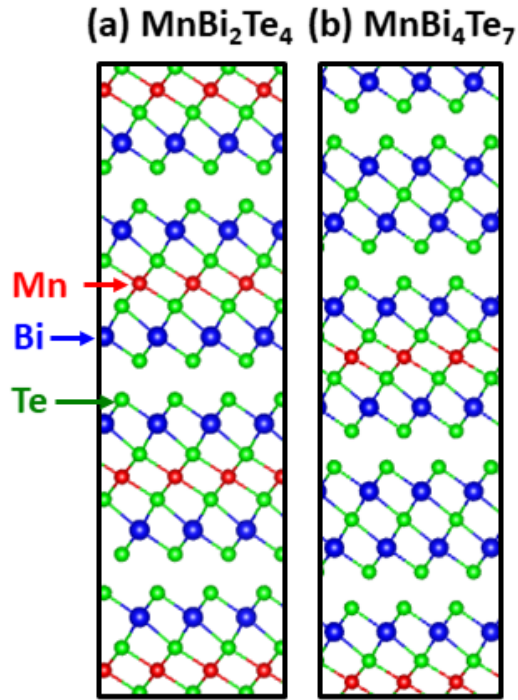


Figure 1. Crystal structures of (a) MnBi_2Te_4 and (b) MnBi_4Te_7 .

The key to the experimental observation of the QAH effect and the axion state is the control of the Fermi level, which needs to be within the bulk band gap. This is, nevertheless, challenging and not realized in MnBi_2Te_4 and MnBi_4Te_7 samples, in which the Fermi level is above the conduction band minimum (CBM) according to the ARPES. Transport measurements show the behavior of degenerate n-type semiconductors,[9,10,12,13,20,22,23] consistent with ARPES results. A frequently used approach to tune the Fermi level is applying a gate voltage to a thin film or a flake in a FET device configuration.[16,17] However, a FET setup is not feasible in all experimental measurements and the Fermi level could be far from the band gap, requiring a very large gate voltage[16], not practical for many device applications. Therefore, the availability of insulating single crystals suitable for various experimental

measurement and device environments is highly desirable. Doping of MnBi_2Te_4 by replacing Bi with isovalent Sb has also been shown to lower the Fermi level, leading to a transition from n- to p-type conductivity in Sb doped MnBi_2Te_4 . [24-26] The Fermi level is tuned to near the valence band maximum (VBM) after replacing about 30% Bi by Sb. [25,26] The drawback of Sb doping is the reduction of the SOC effect and the band gap, [25] which positions the Dirac point closer to band edges, making the transport measurement of surface states more difficult. The AFM MnSb_2Te_4 was shown to be topologically trivial. [25] The Sb doping may also introduce more antisite defects as we discuss in this paper. Doping of MnBi_2Te_4 by electrically active acceptor dopants has not been reported. Previous studies on Bi_2Se_3 show that Ca doping can reduce n-type carrier density and achieve n-to-p type transition in Bi_2Se_3 . [27,28]

MnBi_2Te_4 , MnBi_4Te_7 and $\text{MnBi}_6\text{Te}_{10}$ have high density of defects especially the latter two. Among these three compounds, MnBi_2Te_4 seems to be closest to being stoichiometric with a few percent of antisite disorder, [20,29] although there is a report showing more than 15% Mn deficiency. [21] The Mn deficiency may be sample-dependent. MnBi_4Te_7 and $\text{MnBi}_6\text{Te}_{10}$ are structurally related to MnBi_2Te_4 with the same MnBi_2Te_4 SLs, but have severe Mn deficiencies, which appear to increase with the addition of more Bi_2Te_3 QLs in the unit cell. The Mn deficiencies were estimated to be 15%-20% in MnBi_4Te_7 and 19%-25% in $\text{MnBi}_6\text{Te}_{10}$. [14,21,30] Such high defect densities not only affect the Fermi level but could also influence the magnetic and topological properties. For example, a high density of magnetic defects may affect the surface magnetism and the opening of the surface energy gap. Furthermore, the two

possible surface terminations by either magnetic MnBi_2Te_4 SLs or nonmagnetic Bi_2Te_3 QLs in MnBi_4Te_7 and $\text{MnBi}_6\text{Te}_{10}$ can give rise to two different sets of topological surface states.[14,15,31,32] It is unclear whether the defect concentration varies between SLs and QLs. A detailed study of the defect distribution in MnBi_4Te_7 is highly desirable for understanding and tuning topological surface states.

Despite the critical importance of defect management for synthesis and for the observation of topological quantum states, the defects that cause the nonstoichiometry and the underlying mechanisms behind the apparent different defect chemistries in MnBi_2Te_4 , MnBi_4Te_7 and $\text{MnBi}_6\text{Te}_{10}$ are not well understood. In this paper, we study defect and dopant properties in MnBi_2Te_4 and MnBi_4Te_7 under different growth conditions by density functional theory (DFT) calculations. Defects in MnSb_2Te_4 are also studied as heavy doping of MnBi_2Te_4 by Sb can effectively tune the Fermi level. We show that the antisite defect Bi_{Mn} is the dominant intrinsic donor defects in both MnBi_2Te_4 and MnBi_4Te_7 . Bi_{Mn} cannot be completely compensated by any intrinsic acceptors at the Te-poor limit, leading to the behavior of degenerate n-type semiconductors for both compounds. Adopting a Te-rich condition is predicted to lower the Fermi level. These results are consistent with our transport measurements on MnBi_2Te_4 samples grown with different excess Te contents. In contrast, our defect calculations show that MnSb_2Te_4 is intrinsically p-type with Mn_{Sb} as the dominant acceptor defect. We predict increased defect concentrations from MnBi_2Te_4 , MnBi_4Te_7 , to MnSb_2Te_4 based on our calculations. As a result, heavy Sb doping of MnBi_2Te_4 should induce a higher density of defects, and a high density of magnetic defects Mn_{Sb}

in MnSb_2Te_4 can affect magnetic ordering in MnSb_2Te_4 . Several alkali-metal (Li, Na, K) and alkali-earth-metal (Be, Mg, Ca) dopants are studied in both MnBi_2Te_4 and MnBi_4Te_7 , and Na is found to be the most effective p-type dopant, which can compensate Bi_{Mn} donors, pinning the Fermi level within the band gap even at the Te-poor limit in MnBi_2Te_4 . We also find that the important magnetic defect Mn_{Bi} in MnBi_4Te_7 prefers to form in Bi_2Te_3 QLs and that the MnBi_2Te_4 SL termination has a lower surface energy than the Bi_2Te_3 QL termination. The surprisingly low formation energies of large-size-mismatched antisite defects and dopants and the higher defect concentrations in MnBi_4Te_7 than in MnBi_2Te_4 are explained in the context of strain induced by intercalating MnTe within the Bi_2Te_3 layer.

II. Results

A. Enthalpy of formation and chemical Potentials

The calculated enthalpies of formation for the reactions $\text{MnTe} + \text{Bi}_2\text{Te}_3 \rightarrow \text{MnBi}_2\text{Te}_4$, $\text{MnTe} + 2\text{Bi}_2\text{Te}_3 \rightarrow \text{MnBi}_4\text{Te}_7$, $\text{MnBi}_2\text{Te}_4 + \text{Bi}_2\text{Te}_3 \rightarrow \text{MnBi}_4\text{Te}_7$, and $\text{MnTe} + \text{Sb}_2\text{Te}_3 \rightarrow \text{MnSb}_2\text{Te}_4$ are -5 meV, 5 meV, 10 meV, and 6 meV, respectively. (A negative enthalpy formation indicates exothermic reaction.) These enthalpies of formation are all close to zero (within ± 10 meV), suggesting that synthesis of these compounds can be challenging and that the entropy contribution at elevated temperatures is important to the growth of these ternary compounds. In this paper, the above enthalpies of formation are approximated to zero. As a result, the calculated chemical potential range under thermal equilibrium is represented approximately by a line segment (between

points A and B in Figure 2) rather than a typical polygon because the phase boundaries between the ternary phase (e.g., MnBi_2Te_4) and two binary secondary phases (e.g., MnTe and Bi_2Te_3) overlap when the enthalpy of formation is approximated to zero. The details involved in the calculation of Figure 2 is given in Section V.

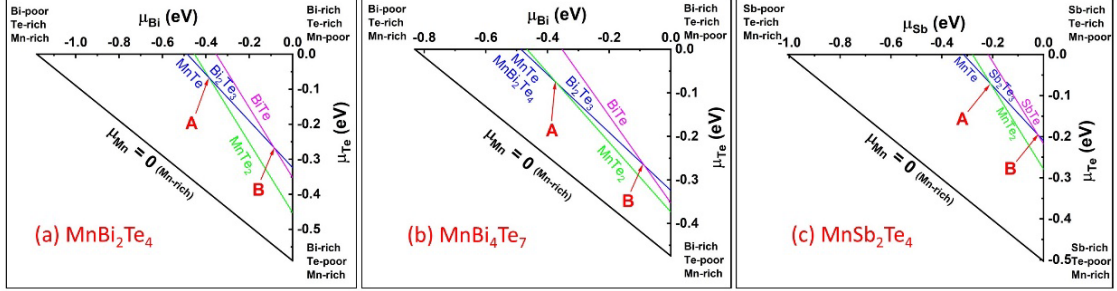


Figure 2. Calculated chemical potential ranges of constituent elements in (a) MnBi_2Te_4 , (b) MnBi_4Te_7 , and (c) MnSb_2Te_4 , respectively. Points A and B correspond to the Te-rich/cation-poor and the Te-poor/cation-rich limits.

B. Intrinsic defects in MnBi_2Te_4 and MnBi_4Te_7

Formation energies of intrinsic point defects, including vacancies, interstitials, and antisites, in MnBi_2Te_4 and MnBi_4Te_7 (with the AFM ordering) are shown in Figures S1 and S2, respectively; the most important low-energy defects are shown in Figures 3 and 4. Some defects can form on several inequivalent sites (such as Mn_{Bi} and Bi_{Te} in MnBi_4Te_7); formation energies for these defects are shown for the energetically most favorable site. As seen in Figures 3 and 4, the antisite defect Bi_{Mn}^+ is the most stable donor defect in both MnBi_2Te_4 and MnBi_4Te_7 . The most important acceptor defects are also antisite defects, i.e., Mn_{Bi}^- and Bi_{Te}^- . Mn_{Bi}^- is the most stable acceptor defect at the Te-rich limit in both compounds. At the Te-poor limit, both Mn_{Bi}^- and Bi_{Te}^- have low formation energies; the former is slightly more stable in MnBi_4Te_7 while the latter

is slightly more stable in MnBi_2Te_4 . Bi_{Te}^- has previously been identified as the dominant acceptor defect at the Te-poor limit in Bi_2Te_3 , [3,33,34] consistent with our results in MnBi_2Te_4 and MnBi_4Te_7 . Vacancies and interstitials all have high formation energies, as shown in Figures S1 and S2, and are not important defects in MnBi_2Te_4 and MnBi_4Te_7 .

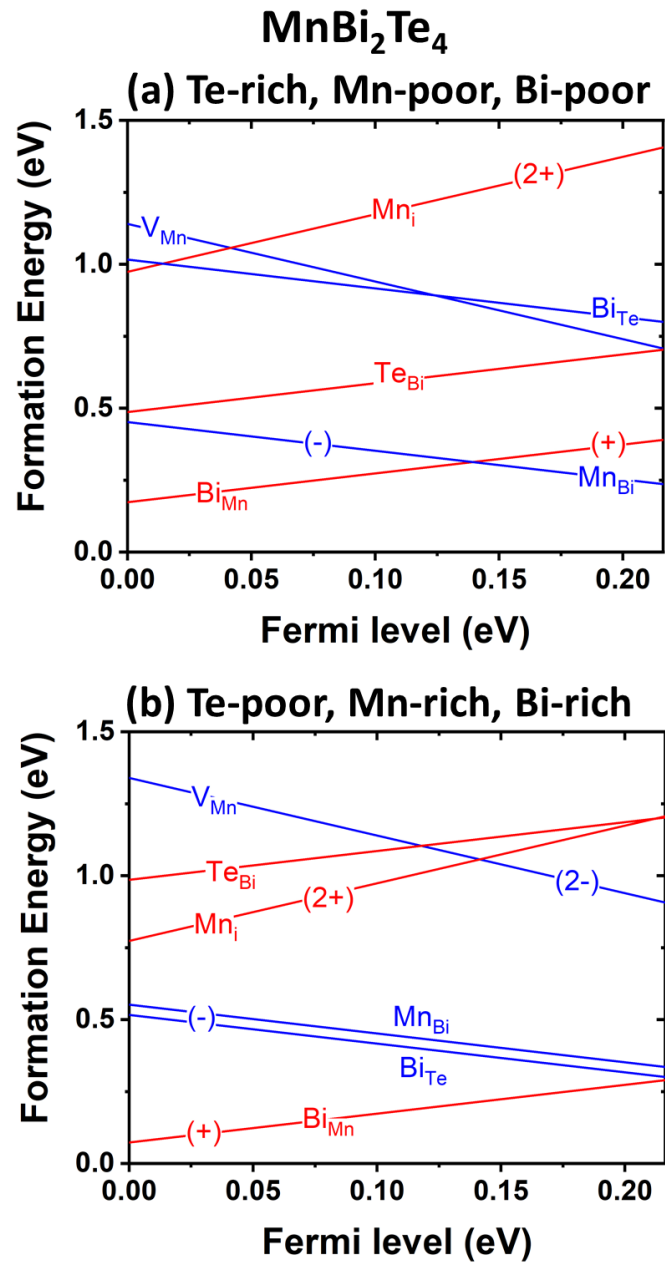


Figure 3. Calculated formation energies of intrinsic defects as functions of the Fermi level (varied from the VBM to the CBM) at the Te-rich/cation-poor (a) and Te-

poor/cation-rich (b) limits [corresponding to points A and B in Figure 2(a), respectively] in MnBi_2Te_4 . The slope of a formation energy line indicates the charge state of the defect as selectively shown.

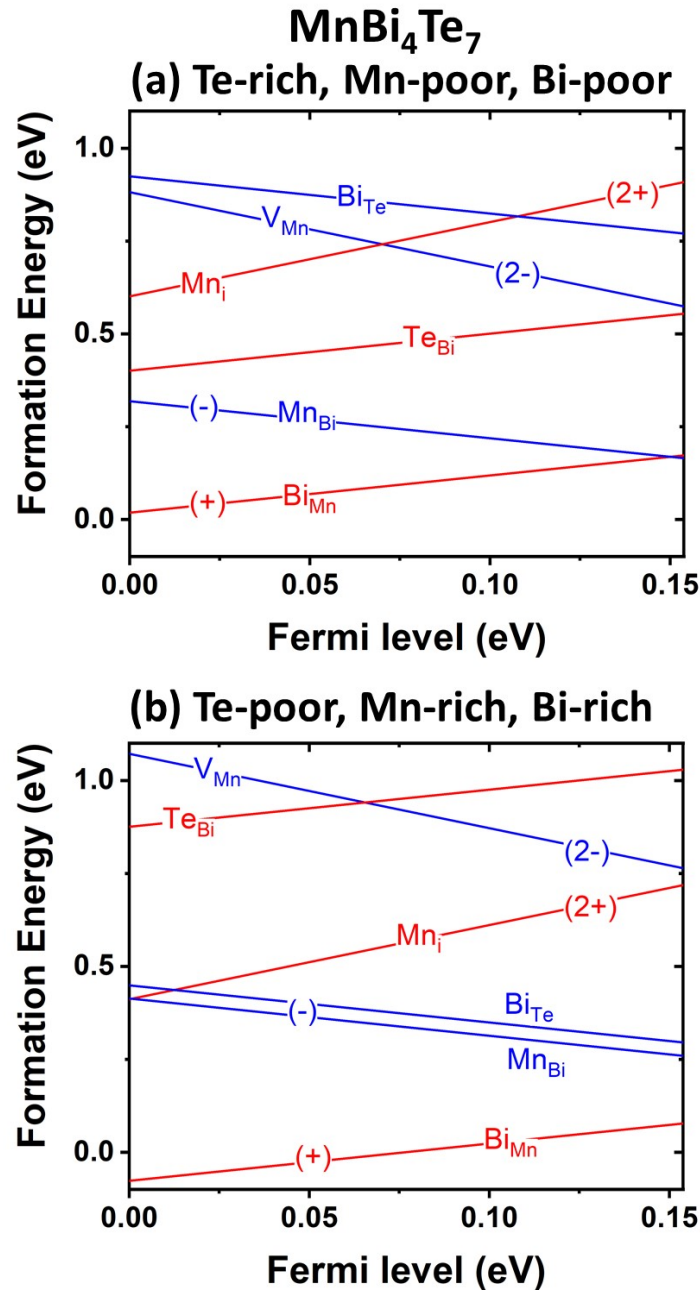


Figure 4. Calculated formation energies of intrinsic defects as functions of the Fermi level (varied from the VBM to the CBM) at the Te-rich/cation-poor (a) and Te-poor/cation-rich (b) limits [corresponding to points A and B in Figure 2(b), respectively] in MnBi_4Te_7 . The slope of a formation energy line indicates the charge state of the

defect as selectively shown.

C. Fermi level and defect concentrations in MnBi_2Te_4 and MnBi_4Te_7

Based on calculated defect formation energies, we further estimate defect and free carrier densities as well as the Fermi level assuming thermal equilibrium and charge neutrality. We calculated defect densities at $T = 585 \text{ }^\circ\text{C}$ (the melting temperature of Bi_2Te_3) by solving Eqs. 9-12 self-consistently. Since the magnetic and topological properties are measured at low temperatures, the Fermi level and the free carrier density at 2 K were then calculated by solving Eqs 9-12 again with the defect densities fixed at the values calculated at $585 \text{ }^\circ\text{C}$. This simulation assumes that defects created at the growth temperature are frozen in the lattice during the subsequent cooling. The implication of this assumption is further discussed below. If there are multiple inequivalent lattice sites for the formation of a defect, formation energies and populations of the defect on all possible sites are considered.

Defect formation energies are strongly affected by elemental chemical potentials, which vary under different experimental growth conditions. Both MnBi_2Te_4 and MnBi_4Te_7 are n-type at the Te-poor limit and p-type at the Te-rich limit as shown in Table I. The significant amount of Bi_{Te} observed on the MnBi_2Te_4 surface by scanning transmission microscopy (STM) [20,29] suggests that the growth condition is likely Te-poor because Bi_{Te} is abundant under only the Te-poor conditions as shown by the calculated formation energies in MnBi_2Te_4 (Figure 3) and MnBi_4Te_7 (Figure 4). Table I also shows that defect densities and the Mn deficiency increases from MnBi_2Te_4 to

MnBi₄Te₇, consistent with the trend observed experimentally. [14,21,30]

Table I. Calculated Fermi level (ϵ_f), free carrier density (and the type of the carrier), as well as densities of the most important intrinsic defects (and concentrations in atomic percent) at both Te-rich and Te-poor limits in MnBi₂Te₄ and MnBi₄Te₇. The Mn:Bi:Te composition ratios calculated based on defect densities are also shown. Bi_{Mn}⁺ and Mn_{Bi}⁻ are important at both Te-rich and Te-poor limits while Bi_{Te}⁻ is important at only the Te-poor limit. The Fermi level is referenced to the valence band maximum (E_V) or the conduction band minimum (E_C). The calculated band gaps of MnBi₂Te₄ and MnBi₄Te₇ are 0.22 eV and 0.15 eV, respectively. Defect densities are calculated at 858.15 K (585 °C) while free carrier densities are calculated at 2 K. The unit of all densities is cm⁻³.

	MnBi ₂ Te ₄		MnBi ₄ Te ₇	
	Te-rich	Te-poor	Te-rich	Te-poor
ϵ_f	$E_V - 0.01$ eV	$E_C + 0.03$ eV	$E_V + 0.06$ eV	$E_C + 0.09$ eV
Carrier density	2.3×10^{19} (p)	8.6×10^{18} (n)	9.6×10^{17} (p)	6.2×10^{19} (n)
[Bi _{Mn} ⁺]	8.1×10^{19} (1.8%)	1.5×10^{20} (3.4%)	4.0×10^{20} (15.7%)	6.0×10^{20} (23.9%)
[Mn _{Bi} ⁻]	1.1×10^{20} (1.2%)	5.6×10^{19} (0.6%)	4.1×10^{20} (4.0%)	2.7×10^{20} (2.6%)
[Bi _{Te} ⁻]		9.0×10^{19} (0.5%)		2.7×10^{20} (1.5%)
Mn:Bi:Te	1.01 : 1.99 : 4	0.98 : 2.05 : 4	1.00 : 4.00 : 7	0.88 : 4.31 : 7

At the Te-poor limit, the calculated Fermi levels in MnBi₂Te₄ ($E_C + 0.03$ eV) and MnBi₄Te₇ ($E_C + 0.09$ eV) are both above the CBM, indicating degenerate n-type conductivities, consistent with ARPES and transport measurements.

[9,10,12,13,20,22,23] Adopting a Te-rich condition lowers the Fermi level in both compounds as shown in Table I. To verify this, we grew MnBi_2Te_4 single crystals out of Bi_2Te_3 flux but with extra Te added. As shown in Figure S3, the electron density decreases with increasing extra Te content in the starting materials, in agreement with the trend found in our calculations. More detailed characterization of these crystals is in progress and will be reported elsewhere.

Despite the agreement in the Fermi level trend between theory and experiment, the Fermi level measured by ARPES is higher ($\sim E_C + 0.2$ eV in both MnBi_2Te_4 and MnBi_4Te_7) [12,31] than the calculated values. The highest calculated Fermi level is obtained at the Te-poor limit ($E_C + 0.03$ eV in MnBi_2Te_4 and $E_C + 0.09$ eV in MnBi_4Te_7). The integration of the DOS from the CBM to $E_C + 0.2$ eV in MnBi_2Te_4 yields a free electron density of $1.6 \times 10^{20} \text{ cm}^{-3}$, in reasonable agreement with our transport measurement based on a sample synthesized with no extra Te in starting materials (see Figure S3). The combination of the DOS calculations with ARPES and transport measurements suggest that the high Fermi level ($\sim E_C + 0.2$ eV) is obtained under a Te-poor condition. The difference in calculated and measured Fermi levels could result from that the thermodynamic condition assumed in calculations is different from that realized in experiments. We calculated all defect densities at $T = 585$ °C under thermal equilibrium. Experimentally, different defects freeze into the crystal lattice at different temperatures during the cooling of the crystal because the diffusivities of different defects differ from each other. MnTe has a much higher melting temperature (1150 °C) than Bi_2Te_3 does (585 °C), indicating stronger Mn-Te chemical bonds than Bi-Te bonds.

Thus, defects on the Mn sublattice may freeze at a higher temperature than those on the Bi sublattice because defect diffusion requires bonding breaking, which could be more difficult in the MnTe sublattice, resulting in higher defect diffusion barriers. This could lead to a larger concentration difference between Bi_{Mn} and Mn_{Bi} than that calculated at an identical temperature as well as a higher measured Fermi level and higher levels of Mn deficiency than the calculated values.

D. Defect segregation and surface termination in MnBi_4Te_7

MnBi_4Te_7 has a more complex structure than MnBi_2Te_4 as shown in Figure 1. The separation of magnetic MnBi_2Te_4 SLs by nonmagnetic Bi_2Te_3 QLs reduces AFM coupling, allowing more freedom in manipulating magnetic and topological properties[10,15,35]. Here, we investigate defect distributions and surface terminations in MnBi_4Te_7 .

In MnBi_4Te_7 , the low-energy acceptor defects Mn_{Bi}^- and Bi_{Te}^- can form in either a MnBi_2Te_4 SL or a Bi_2Te_3 QL. There are two inequivalent sites for Bi_{Te}^- (six- and three-fold coordination) and one site for Mn_{Bi}^- in each SL or QL. The relative energies of Mn_{Bi}^- and Bi_{Te}^- on these different sites are shown in Table II. The formation of Mn_{Bi}^- in the SL is energetically more favorable than in the QL by 0.12 eV. On the other hand, Bi_{Te}^- favors the three-fold coordinated Te site but has little preference on whether this site is in the SL or QL. Therefore, Bi_{Te}^- is distributed in both the SL and QL with nearly the same probability while Mn_{Bi}^- prefers segregation into the QL in MnBi_4Te_7 . Based on calculated formation energies of Mn_{Bi}^- on different sites, it can

be shown that about 5/6 and 1/6 of Mn_{Bi}^- are located in the QL and SL, respectively.

Surface energies of MnBi_2Te_4 - and Bi_2Te_3 -terminated surfaces in MnBi_4Te_7 are calculated (using Eq. 13) to be 0.19 eV and 0.21 eV per surface unit cell. Thus, the MnBi_2Te_4 -terminated surface is more stable. The magnetic Mn_{Bi} defects are expected to be reduced from this surface due to the gettering effect of Bi_2Te_3 QLs as discussed above. However, even 1/6 of the total Mn_{Bi}^- population in SLs is significant. At the Te-poor limit, 0.9% of Bi ions are replaced by Mn in SLs, compared to 4.4% replacement in QLs.

Table II. Formation energies of Mn_{Bi}^- and Bi_{Te}^- on different sites in MnBi_4Te_7 . There are two sites for Bi_{Te}^- (six- and three-fold coordination) and one site (six-fold coordination) for Mn_{Bi}^- in each SL MnBi_2Te_4 or Bi_2Te_3 QL. The energy for the most stable site for each defect is set to zero. The unit is in eV.

	MnBi_2Te_4 SL		Bi_2Te_3 QL	
	Six-fold	Three-fold	Six-fold	Three-fold
Mn_{Bi}^-	0.12	N/A	0	N/A
Bi_{Te}^-	0.75	< 0.01	0.55	0

E. Intrinsic defects in MnSb_2Te_4

MnBi_2Te_4 and MnBi_4Te_7 are degenerate n-type semiconductors at the Te-poor limit as shown in Table I. Heavy Sb doping (~30%) has been used to lower the Fermi level, leading to a transition from n- to p-type conductivity in Sb doped MnBi_2Te_4 . [24-26] We studied intrinsic defects in MnSb_2Te_4 (with the AFM ordering) to better understand the effect of Sb doping in MnBi_2Te_4 . The calculated band gap of AFM MnSb_2Te_4 is very

small (11 meV), in agreement with a previous study[25]. Thus, we show only the formation energies of the important intrinsic defects at the VBM at both the Te-rich and -poor limits in Table III. There are two important differences between intrinsic defects in MnSb_2Te_4 and those in MnBi_2Te_4 . (1) MnSb_2Te_4 favors the formation of acceptor defects (Mn_{Sb}^- and Sb_{Te}^-) over the donor defect Sb_{Mn}^+ , consistent with the transition from n- to p-type conductivity observed in Sb doped MnBi_2Te_4 . [24] (2) The calculated formation energy of an isolated Mn_{Sb}^- is slightly negative, indicating spontaneous formation of Mn_{Sb}^- under thermal equilibrium. Therefore, pure MnSb_2Te_4 should have a very high defect density and heavy Sb doping of MnBi_2Te_4 should increase the concentration of magnetic defects, which can potentially affect the bulk and surface magnetism. The contradictory experimental reports of magnetic ordering in MnSb_2Te_4 (AFM in Ref. [24] and FM in Ref. [36]) might be caused by different samples with different Mn_{Sb}^- densities and distributions. A high density of Mn_{Sb}^- could lead to magnetic ordering of Mn_{Sb}^- defects, which mediates a FM interlayer coupling in bulk MnSb_2Te_4 . [36]

Table III. Calculated formation energies of low-energy intrinsic defects in MnSb_2Te_4 at both Te-rich and Te-poor limits [corresponding to points A and B in Figure 2(c)]. The unit is in eV.

	Sb_{Mn}^+	Mn_{Sb}^-	$\text{Sb}_{\text{Mn}}-\text{Mn}_{\text{Sb}}$	Sb_{Te}^-	V_{Mn}^{2-}
Te-rich	0.43	-0.06	0.08	0.40	0.37
Te-poor	0.37	-0.01	0.08	0.08	0.50

F. Chemical Doping

As shown in Table I as well as in Figures 3, 4, S3, a Te-rich condition can lower the Fermi level. However, an extremely Te-rich condition close to the Te-rich limit may not be accessible in experiment and the kinetic effect may lead to a higher freeze-in temperature for Bi_{Mn}^+ compared to that of Mn_{Bi}^- , favoring a higher Fermi level as discussed in Sec. II-C. Here, we study extrinsic acceptor dopants, including alkali metal (Li, Na, K) and alkali-earth metal (Be, Mg, Ca) dopants, in MnBi_2Te_4 and MnBi_4Te_7 . We investigated all above dopants in MnBi_4Te_7 for its small unit cell, and the most effective acceptor dopant was further studied in MnBi_2Te_4 .

Among the investigated alkali metal and alkali-earth metal dopants, Na is found to be the most effective p-type dopant. Figures 5 and 6 show calculated formation energies of substitutional Na_{Mn}^- and $\text{Na}_{\text{Bi}}^{2-}$ as well as interstitial Na_i^+ in MnBi_2Te_4 and MnBi_4Te_7 . It can be seen that Na_{Mn}^- has a lower formation energy than $\text{Na}_{\text{Bi}}^{2-}$, Na_i^+ , and the most stable intrinsic acceptor defect; therefore, Na_{Mn}^- can act as the dominant acceptor, which compensates the intrinsic donor defect Bi_{Mn}^+ , at both Te-rich and -poor limits in both MnBi_2Te_4 and MnBi_4Te_7 .

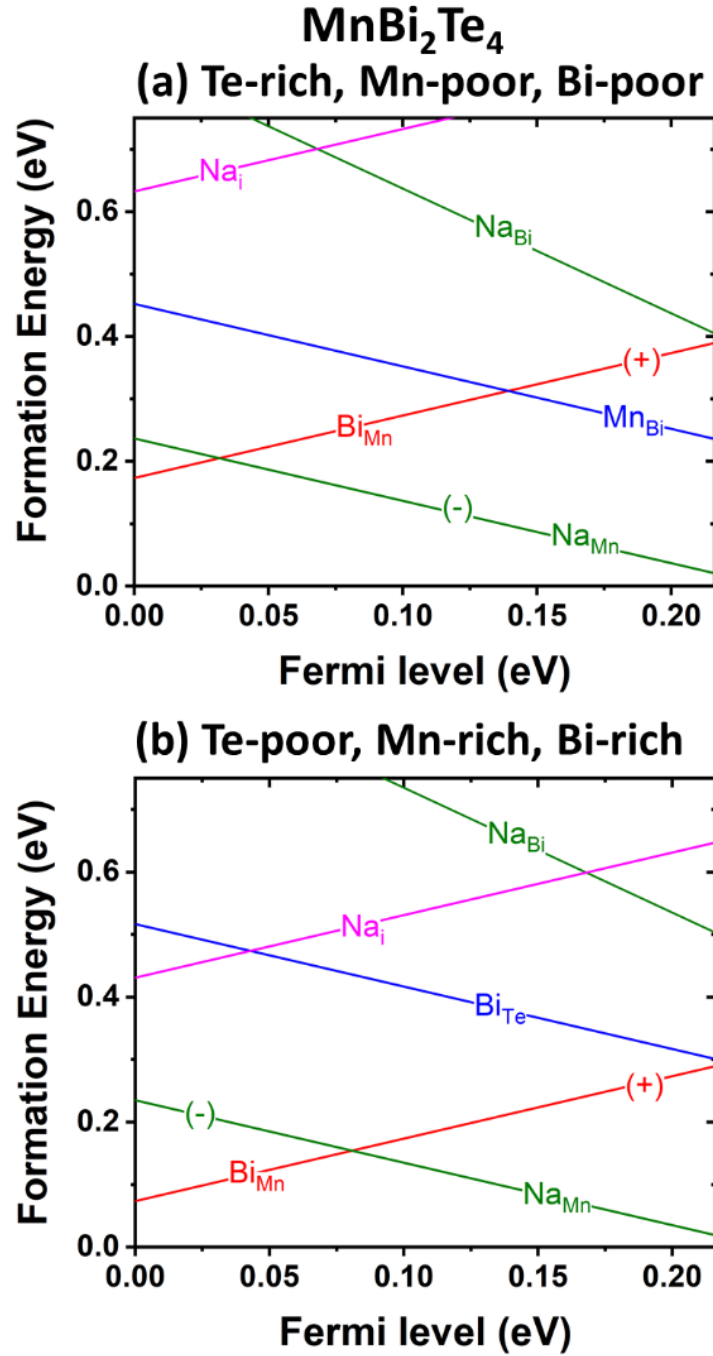


Figure 5. Calculated formation energies of Na_{Mn}^- , $\text{Na}_{\text{Bi}}^{2-}$, Na_i^+ , and the most stable intrinsic defects as functions of the Fermi level (varied from the VBM to the CBM) at the Te-rich/cation-poor (a) and Te-poor/cation-rich (b) limits [corresponding to points A and B in Figure 2(a), respectively] in MnBi_2Te_4 . The Na-rich limit is applied in both (a) and (b). The slope of a formation energy line indicates the charge state of the defect as selectively shown.

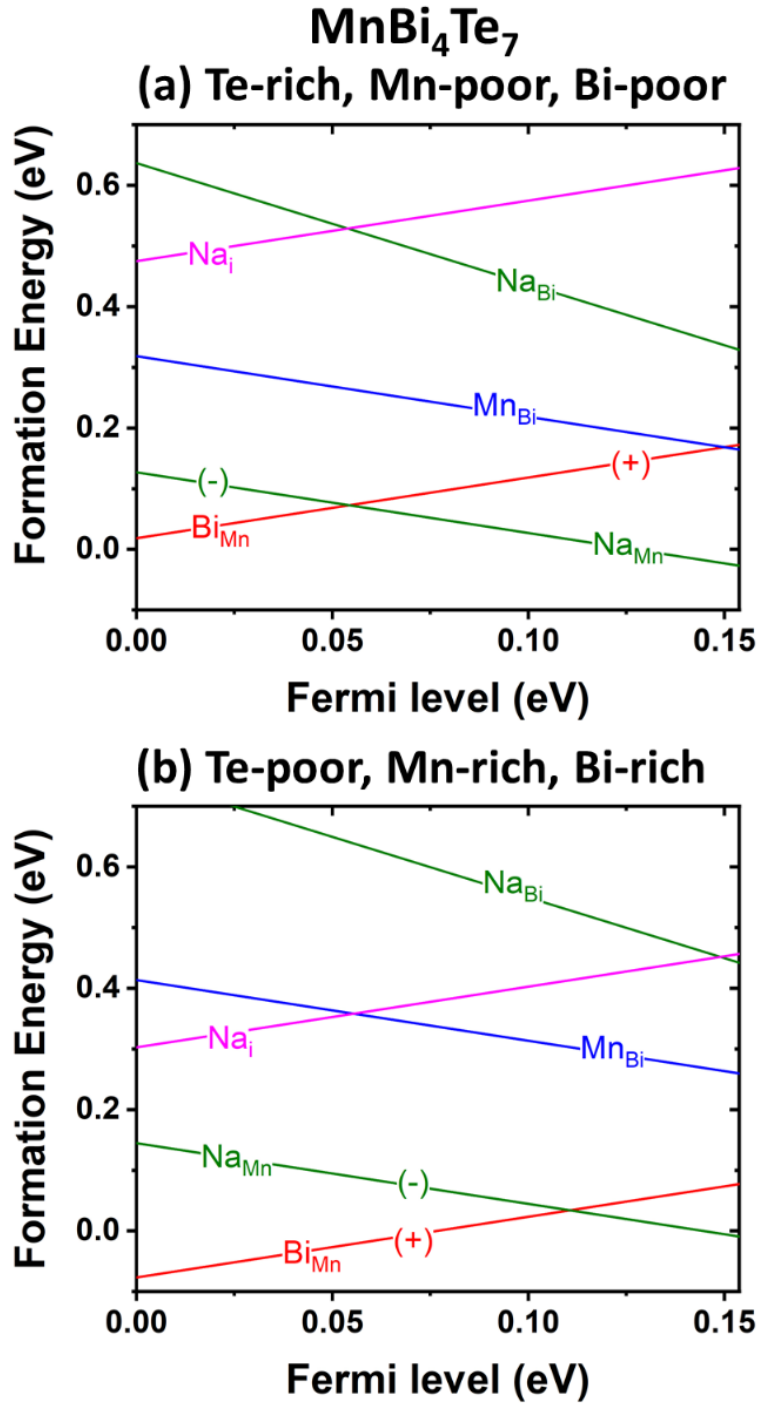


Figure 6. Calculated formation energies of Na_{Mn}^- , $\text{Na}_{\text{Bi}}^{2-}$, Na_i^+ , and the most stable intrinsic defects as functions of the Fermi level (varied from the VBM to the CBM) at the Te-rich/cation-poor (a) and Te-poor/cation-rich (b) limits [corresponding to points A and B in Figure 2(b), respectively] in MnBi_4Te_7 . The Na-rich limit is applied in both (a) and (b). The slope of a formation energy line indicates the charge state of the defect as selectively shown.

As shown in Table I, both MnBi_2Te_4 and MnBi_4Te_7 can be tuned p-type at the Te-rich limits. However, the experimental growth condition appears to be close to the Te-poor limit, resulting in the Fermi level above the CBM as discussed in Sec. II-C. Thus, we focus on Na doping at the Te-poor limit. Formation energies of Na dopants shown in Figures 5-6 are the lowest values calculated at the Na-rich limit [highest Na chemical potential allowed by Eq. (8)]. At the Na-rich and Te-poor limits, the calculated $[\text{Na}_{\text{Mn}}^-]$ and $[\text{Bi}_{\text{Mn}}^+]$ are $5.7 \times 10^{20} \text{ cm}^{-3}$ (12.6%) and $5.5 \times 10^{20} \text{ cm}^{-3}$ (12.3%), respectively, in MnBi_2Te_4 and $1.5 \times 10^{21} \text{ cm}^{-3}$ (59.7%) and $1.7 \times 10^{21} \text{ cm}^{-3}$ (66.9%), respectively, in MnBi_4Te_7 . These are very high densities. In the case of MnBi_4Te_7 , the calculated defect and dopant densities are unrealistic; thus, calculations of the formation energy of an isolated defect/dopant [Eq. (8)] and its density [Eq. (9)] cannot be applied to the case of high defect/dopant densities at the Na-rich/Te-poor limit.

To better understand the effect of Na doping, we studied a range of lower Na doping levels below the solid solubility of Na, and calculated densities of free carriers, intrinsic defects and the Fermi level as functions of $[\text{Na}_{\text{Mn}}^-]$ at the Te-poor limit in both MnBi_2Te_4 and MnBi_4Te_7 (see Figure 7). In MnBi_2Te_4 , 1.6% of Na_{Mn}^- doping ($7 \times 10^{19} \text{ cm}^{-3}$) can position the Fermi level near the midgap ($E_V + 0.09 \text{ eV}$), at which $[\text{Bi}_{\text{Mn}}^+]$ is about 4.2% ($1.88 \times 10^{19} \text{ cm}^{-3}$) [see Figure 7(a)]. On the other hand, the Fermi level in MnBi_4Te_7 remains above the CBM despite heavy Na doping [up to nearly 40% ($1 \times 10^{21} \text{ cm}^{-3}$)] as shown in Figure 7(b). Therefore, Na doping can lead to the insulating behavior in MnBi_2Te_4 even at the Te-poor limit but must be combined with a more Te-rich growth condition to lower the Fermi level into the band gap in MnBi_4Te_7 .

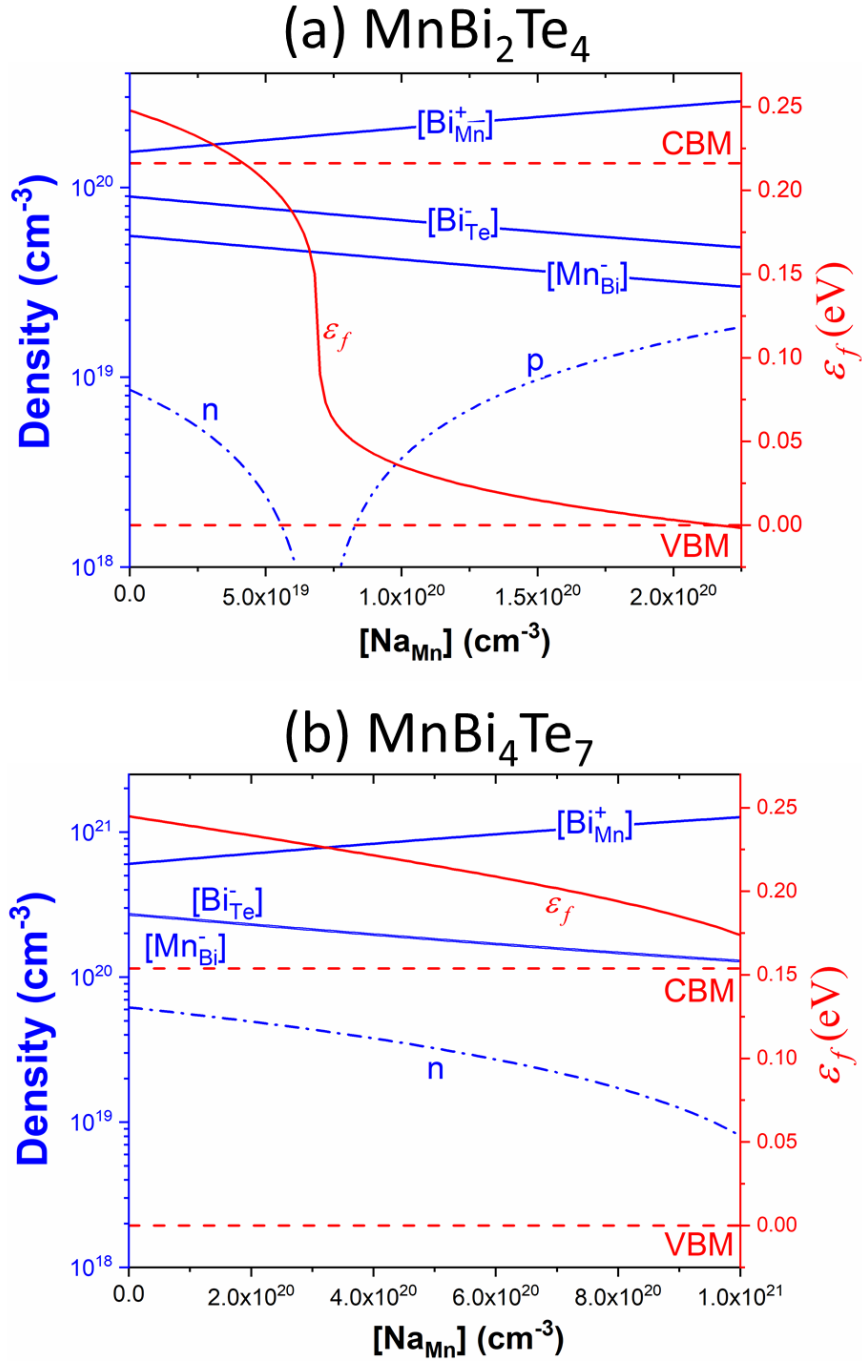


Figure 7. Densities of free electrons (n) and holes (p) and most important intrinsic defects (in blue) as well as the Fermi level (in red) as functions of the substitutional Na_{Mn} density calculated at the Te-poor limit in (a) MnBi_2Te_4 and (b) MnBi_4Te_7 . The densities of native Mn ions are $4.49 \times 10^{21} \text{ cm}^{-3}$ and $2.53 \times 10^{21} \text{ cm}^{-3}$ in MnBi_2Te_4 and MnBi_4Te_7 , respectively.

III. Discussion

A. Large-size-mismatched antisite defects and substitutional dopants

Our defect calculations show that Bi_{Mn} has a very low formation energy in MnBi_2Te_4 and MnBi_4Te_7 especially in the latter (Figures 3-4) despite that the ionic radius of Bi^{3+} (1.03 Å) is much larger than that of Mn^{2+} (0.83 Å).[37] The stability of such large-sized-mismatched antisite defect is likely related to strain in the MnTe layer. The MnTe layer is intercalated within the Bi_2Te_3 layer in a SL, forming a natural internal heterostructure. The calculated in-plane lattice constants of hexagonal lattices of MnTe, MnBi_2Te_4 , MnBi_4Te_7 , and Bi_2Te_3 increase from 4.160 Å, 4.365 Å, 4.394 Å to 4.433 Å. These results suggest that the MnTe layer is under significant tensile strain in MnBi_2Te_4 . Such strain is further increased in MnBi_4Te_7 because an additional Bi_2Te_3 QL in the unit cell of MnBi_4Te_7 expands the in-plane lattice constant. Therefore, substitution of Mn by a large ion reduces the tensile strain in the MnTe layer. This could explain the low formation energy of Bi_{Mn} . Opposite to the tensile strain in the inner MnTe layer, the outer Bi_2Te_3 layer that encapsulates the MnTe layer is under the compressive strain, which promotes the substitution of Bi by a smaller Mn ion. However, the Bi_2Te_3 layer is thicker and adjacent to the vdW gap; thus, the strain in the Bi_2Te_3 layer is better relaxed than that in the MnTe layer. This is consistent with the generally lower formation energy of Bi_{Mn} than that of Mn_{Bi} . Compared to MnBi_2Te_4 , the tensile strain in the MnTe layer is larger and the compressive strain in the Bi_2Te_3 layer is smaller in MnBi_4Te_7 , resulting in a lower Bi_{Mn} formation energy and a higher Mn_{Bi} formation energy (hence, increased Mn deficiency) in MnBi_4Te_7 . Based on the above analysis, it

may be expected that $\text{MnBi}_6\text{Te}_{10}$, which has two Bi_2Te_3 QLs in the unit cell, should have more Bi_{Mn} and less Mn_{Bi} than MnBi_4Te_7 and MnBi_2Te_4 . Indeed, previous experiments showed an increased Mn deficiency in $\text{MnBi}_6\text{Te}_{10}$. [21,30]

The strain effect described above also determines the doping efficiency. Substitutional doping usually favors dopants with sizes close to that of the substituted native atom. However, due to the tensile strain in the MnTe layer, a large-sized dopant with the size close to that of Bi is favored on the Mn site. Similarly, due to the compressive strain in the Bi_2Te_3 layer, a small-sized dopant with the size close to that of Mn is favored on the Bi site. This is demonstrated by alkali-metal doping in MnBi_4Te_7 as shown in Figure 8. Li^+ has an ionic radius of 0.76 Å, close to that of Mn^{2+} (0.83 Å) while Na^+ has an ionic radius of 1.02 Å, close to that of Bi^{3+} (1.03 Å). [37] Nevertheless, the large-size-mismatched Na_{Mn}^- has a lower formation energy than Li_{Mn}^- . K_{Mn}^- has a very high formation energy because K^+ has an ionic radius of 1.38 Å, even much larger than the size of Bi^{3+} . Turning to alkali-earth-metal dopants, the size of Ca^{2+} (1 Å) is close to that of Bi^{3+} (1.03 Å) and the size of Mg^{2+} (0.72 Å) is close to that of Mn^{2+} (0.83 Å). [37] Again, the large-size-mismatched Mg_{Bi}^- has a lower formation energy than Ca_{Bi}^- in MnBi_4Te_7 as shown in Figure 9. We have also tested Be_{Bi}^- . The small ionic radius of Be^{2+} (0.45 Å) causes the off centering of the Be ion on the Bi site, leading to a very high formation energy (not shown). Figure 9 also shows that alkali-earth-metal dopants favor the doping on the isovalent Mn site, rendering them electrically inactive and ineffective in tuning the Fermi level.

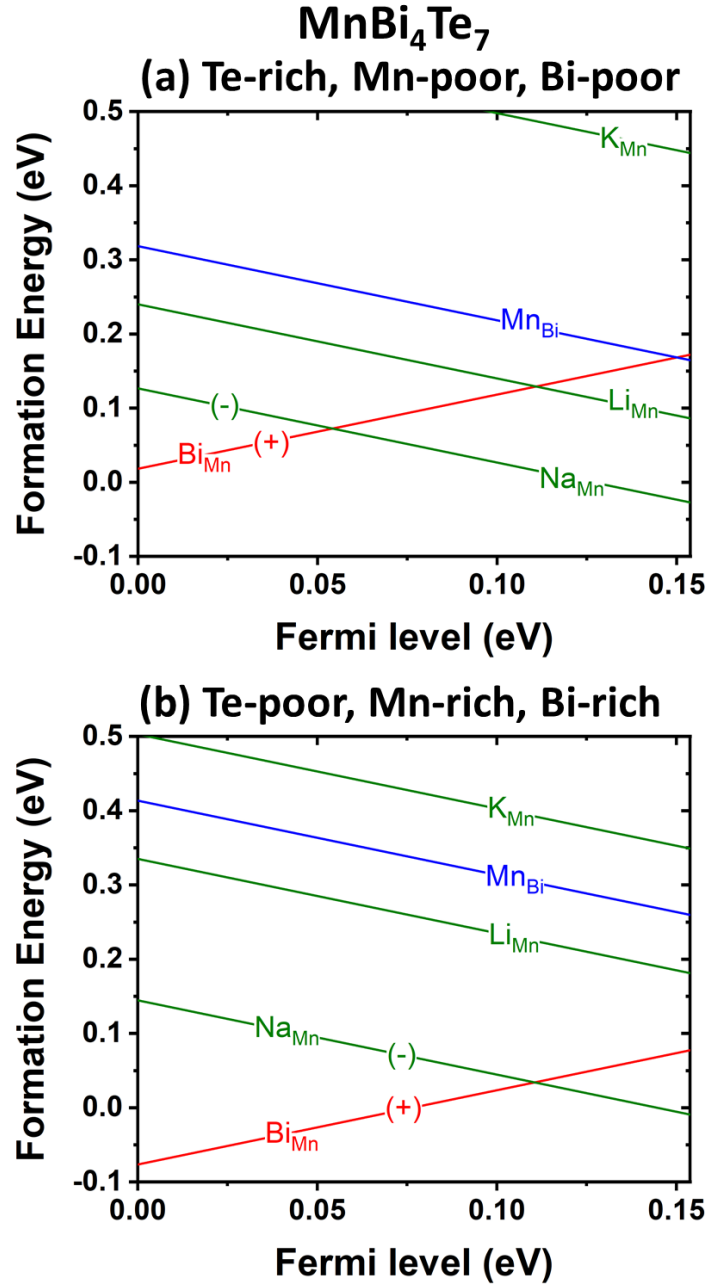


Figure 8. Calculated formation energies of Li_{Mn}^- , Na_{Mn}^- , K_{Mn}^- , and the most stable intrinsic defects as functions of the Fermi level (varied from the VBM to the CBM) at the Te-rich/cation-poor (a) and Te-poor/cation-rich (b) limits [corresponding to points A and B in Figure 2(b), respectively] in MnBi_4Te_7 . The dopant-rich limit is applied in both (a) and (b). The slope of a formation energy line indicates the charge state of the defect as selectively shown.

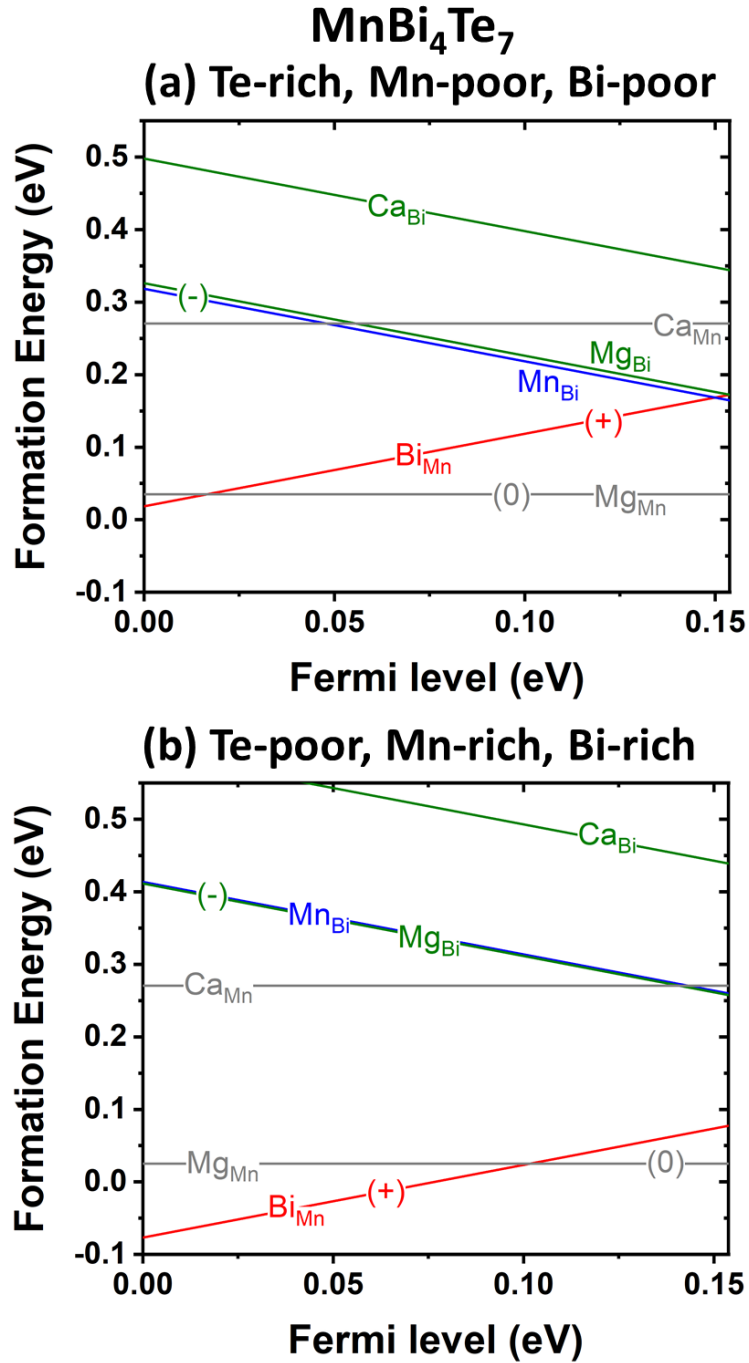


Figure 9. Calculated formation energies of substitutional Mg and Ca dopants and the most stable intrinsic defects as functions of the Fermi level (varied from the VBM to the CBM) at the Te-rich/cation-poor (a) and Te-poor/cation-rich (b) limits [corresponding to points A and B in Figure 2(b), respectively] in MnBi₄Te₇. The dopant-rich limit is applied in both (a) and (b). The slope of a formation energy line indicates the charge state of the defect as selectively shown.

B. Composition analysis

Our defect calculations shown in Sec. II-B and C suggest that several assumptions made in the experimental composition analysis [14,21,30] could lead to significant errors. (1) The charge state of Bi ions was assumed to be +3 when the charge neutrality condition was applied in the composition analysis. However, the Bi ion in Bi_{Te}^- has a charge state of -1 and Bi_{Te}^- is abundant and has a density comparable to that of Mn_{Bi}^- in both MnBi_2Te_4 and MnBi_4Te_7 at the Te-poor limit (Table I). (2) Previous composition analyses did not consider the free carrier density when applying the charge neutrality condition. However, the free electron density can be on the order of 10^{20} cm^{-3} (Figure S3), comparable to defect densities. (3) The Mn vacancy, V_{Mn}^{2-} , which was assumed as an important defect in previous composition analyses, actually has a relatively high formation energy in both MnBi_2Te_4 and MnBi_4Te_7 (Figures 3-4) and should not be a major factor behind the experimentally observed Mn deficiency in MnBi_4Te_7 [14,21,30]. The neglect of the negatively charged Bi_{Te}^- and free electrons could increase the estimated density of positively charged defects (Bi_{Mn}^+), leading to artificially high Mn deficiencies in composition analyses.

IV. Conclusion

We show that the intercalation of the MnTe layer within the Bi_2Te_3 layer in antiferromagnetic topological insulators MnBi_2Te_4 and MnBi_4Te_7 creates an internal heterostructure with large strain, promoting the formation of large-size-mismatched antisite defect Bi_{Mn} , which is shown to be more abundant in MnBi_4Te_7 than in MnBi_2Te_4

due to the larger tensile strain in the MnTe layer in the former. The abundance of the intrinsic donor defect Bi_{Mn} positions the Fermi level above the CBM under the Te-poor growth condition, giving rise to n-type metallic conductivity. Our DFT calculations and preliminary synthesis demonstrate that adopting a Te-rich condition can lower the Fermi level, which may be pinned inside the bulk energy gap of MnBi_2Te_4 and MnBi_4Te_7 – a condition needed for quantum transport measurement of surface states. In contrast, the intrinsic acceptor defect Mn_{Sb} is dominant in MnSb_2Te_4 , leading to p-type conductivity. The strain at the internal heterostructure also enables the efficient incorporation of large-size-mismatched substitutional acceptor dopant Na_{Mn} , which can have a density higher than any intrinsic defects. We show that Na_{Mn} can compensate Bi_{Mn} and pin the Fermi level inside the band gap even at the Te-poor limit in MnBi_2Te_4 . The high density of magnetic defects (Mn_{Bi} in MnBi_2Te_4 and MnBi_4Te_7 and Mn_{Sb} in MnSb_2Te_4) found in this study may have important implications to magnetic and topological properties and deserve further studies.

V. Methods

A. Defect and dopant formation energy calculations

The formation energy of a defect or a dopant is given by

$$\Delta H(q, \varepsilon_f) = (E_D - E_h) - \sum_i n_i (\mu_i + \mu_i^{\text{bulk}}) + q(\varepsilon_{VBM} + \varepsilon_f), \quad (1)$$

where E_D and E_h are the total energies of the defect-containing and the host (i.e. defect-free) supercells. The formation of a defect in a material involves an exchange of atoms with their respective chemical reservoirs. The second term in Eq. (1) represents

the change in energy due to such exchange of atoms, where n_i is the difference in the number of atoms for the i 'th atomic species between the defect-containing and defect-free supercells. μ_i is the relative chemical potential for the i 'th atomic species, referenced to the chemical potential of its elemental bulk phase μ_i^{bulk} . The third term in Eq. (1) represents the change in energy due to the exchange of electrons with its reservoir. q is the charge state of the defect. ε_{VBM} is the energy of the VBM and ε_f is the Fermi energy relative to the VBM. The correction to the defect formation energy due to potential alignment (between the host and a charged defect supercell) [38] was applied. The image charge correction was not included because the supercell size along the c axis and the static dielectric constant on the a - b plane are very large, suppressing the image charge interaction. [The supercell sizes along c are 80.951 Å for MnBi_2Te_4 , 47.267 Å for MnBi_4Te_7 , and 80.601 Å for MnSb_2Te_4 . The calculated static dielectric constant on the a - b plane of MnBi_4Te_7 is 225 (the electronic and ionic contributions are 107 and 118, respectively.) The dielectric constants of MnBi_2Te_4 and MnSb_2Te_4 are expected to be large as well.]

The chemical potentials in Eq. (1) are subject to a series of thermodynamic constraints under the equilibrium growth condition. To maintain the stability of MnBi_2Te_4 during growth, the chemical potentials of Mn, Bi, and Te should satisfy

$$\mu_{\text{Mn}} + 2\mu_{\text{Bi}} + 4\mu_{\text{Te}} = \Delta H(\text{MnBi}_2\text{Te}_4), \quad (2)$$

where $\Delta H(\text{MnBi}_2\text{Te}_4)$ is the enthalpy of formation for MnBi_2Te_4 . Eq. 2 reduces the number of independent elemental chemical potentials to two. We chose μ_{Bi} and μ_{Te} as the two independent elemental chemical potentials to plot Figure 2. μ_{Mn} can be

determined by Eq. 2.

To avoid the formation of binary phases (MnTe, MnTe₂, Bi₂Te₃, BiTe, Bi₄Te₃, Bi₈Te₉) and elemental phases of Mn, Bi, and Te, the following constraints on chemical potentials are applied:

$$\begin{aligned}
\mu_{\text{Mn}} + \mu_{\text{Te}} &\leq \Delta H(\text{MnTe}), \\
\mu_{\text{Mn}} + 2\mu_{\text{Te}} &\leq \Delta H(\text{MnTe}_2), \\
2\mu_{\text{Bi}} + 3\mu_{\text{Te}} &\leq \Delta H(\text{Bi}_2\text{Te}_3), \\
\mu_{\text{Bi}} + \mu_{\text{Te}} &\leq \Delta H(\text{BiTe}), \\
4\mu_{\text{Bi}} + 3\mu_{\text{Te}} &\leq \Delta H(\text{Bi}_4\text{Te}_3), \\
8\mu_{\text{Bi}} + 9\mu_{\text{Te}} &\leq \Delta H(\text{Bi}_8\text{Te}_9), \\
\mu_{\text{Mn}} \leq 0, \mu_{\text{Bi}} \leq 0, \mu_{\text{Te}} &\leq 0.
\end{aligned} \tag{3}$$

Here, $\Delta H(\text{MnTe})$, $\Delta H(\text{MnTe}_2)$, $\Delta H(\text{Bi}_2\text{Te}_3)$, $\Delta H(\text{BiTe})$, $\Delta H(\text{Bi}_4\text{Te}_3)$, and $\Delta H(\text{Bi}_8\text{Te}_9)$ are enthalpies of formation for MnTe, MnTe₂, Bi₂Te₃, BiTe, Bi₄Te₃, and Bi₈Te₉, respectively.

For the growth of MnBi₄Te₇, the chemical potentials of Mn, Bi, and Te should satisfy

$$\mu_{\text{Mn}} + 4\mu_{\text{Bi}} + 7\mu_{\text{Te}} = \Delta H(\text{MnBi}_4\text{Te}_7), \tag{4}$$

where $\Delta H(\text{MnBi}_4\text{Te}_7)$ is the enthalpy of formation for MnBi₄Te₇. All chemical potential constraints in Eq. (3) also apply to MnBi₄Te₇ with an additional constraint for avoiding the formation of MnBi₂Te₄:

$$\mu_{\text{Mn}} + 2\mu_{\text{Bi}} + 4\mu_{\text{Te}} \leq \Delta H(\text{MnBi}_2\text{Te}_4). \tag{5}$$

For the growth of MnSb₂Te₄, the chemical potentials of Mn, Sb, and Te should

satisfy

$$\mu_{\text{Mn}} + 2\mu_{\text{Sb}} + 4\mu_{\text{Te}} = \Delta H(\text{MnSb}_2\text{Te}_4), \quad (6)$$

where $\Delta H(\text{MnSb}_2\text{Te}_4)$ is the enthalpy of formation for MnSb_2Te_4 . The following constraints are applied to avoid the formation of secondary phases (MnTe , MnTe_2 , Sb_2Te_3 , SbTe , Sb_2Te , Sb_8Te_3 , Mn , Sb , Te):

$$\begin{aligned} \mu_{\text{Mn}} + \mu_{\text{Te}} &\leq \Delta H(\text{MnTe}), \\ \mu_{\text{Mn}} + 2\mu_{\text{Te}} &\leq \Delta H(\text{MnTe}_2), \\ 2\mu_{\text{Sb}} + 3\mu_{\text{Te}} &\leq \Delta H(\text{Sb}_2\text{Te}_3), \\ \mu_{\text{Sb}} + \mu_{\text{Te}} &\leq \Delta H(\text{SbTe}), \\ 2\mu_{\text{Sb}} + \mu_{\text{Te}} &\leq \Delta H(\text{Sb}_2\text{Te}), \\ 8\mu_{\text{Sb}} + 3\mu_{\text{Te}} &\leq \Delta H(\text{Sb}_8\text{Te}_3), \\ \mu_{\text{Mn}} &\leq 0, \mu_{\text{Sb}} \leq 0, \mu_{\text{Te}} \leq 0. \end{aligned} \quad (7)$$

Here, $\Delta H(\text{Sb}_2\text{Te}_3)$, $\Delta H(\text{SbTe})$, $\Delta H(\text{Sb}_2\text{Te})$, and $\Delta H(\text{Sb}_8\text{Te}_3)$ are enthalpies of formation for Sb_2Te_3 , SbTe , Sb_2Te , and Sb_8Te_3 , respectively.

After considering all above constraints, we find that the stable phase of MnBi_2Te_4 is confined by MnTe , MnTe_2 , Bi_2Te_3 , and BiTe phases [Figure 2(a)]; the stable phase of MnBi_4Te_7 is confined by MnTe , MnTe_2 , Bi_2Te_3 , BiTe , and MnBi_2Te_4 phases [Figure 2(b)]; the stable phase of MnSb_2Te_4 is confined by MnTe , MnTe_2 , Sb_2Te_3 , and SbTe phases [Figure 2(c)]. Other phases considered in Eqs (3) and (7) do not share boundaries with the targeted ternary phase and thus are not shown in Figure 2. It is shown in Sec. II-A that MnBi_2Te_4 is marginally stable against decomposition to MnTe and Bi_2Te_3 whereas MnBi_4Te_7 and MnSb_2Te_4 are slightly metastable compared to binary phases

(all by a few meV, close to the numerical uncertainty). To simplify the problem, we make following approximations: $\Delta H(\text{MnTe}) + \Delta H(\text{Bi}_2\text{Te}_3) = \Delta H(\text{MnBi}_2\text{Te}_4)$, $\Delta H(\text{MnTe}) + 2\Delta H(\text{Bi}_2\text{Te}_3) = \Delta H(\text{MnBi}_4\text{Te}_7)$, $\Delta H(\text{MnBi}_2\text{Te}_4) + \Delta H(\text{Bi}_2\text{Te}_3) = \Delta H(\text{MnBi}_4\text{Te}_7)$, and $\Delta H(\text{MnTe}) + \Delta H(\text{Sb}_2\text{Te}_3) = \Delta H(\text{MnSb}_2\text{Te}_4)$. As a result, the chemical potential ranges in MnBi_2Te_4 , MnBi_4Te_7 and MnSb_2Te_4 are line segments as shown in the phase diagrams of Figure 2, which introduces errors of a few meV.

Chemical doping of MnBi_2Te_4 and MnBi_4Te_7 by Li, Na, K, Be, Mg, and Ca are limited by the formation of dopant-Te secondary phases. The following constraints are, thus, applied:

$$\begin{aligned}
2\mu_{\text{Li}} + \mu_{\text{Te}} &\leq \Delta H(\text{Li}_2\text{Te}), \\
\mu_{\text{Li}} + 3\mu_{\text{Te}} &\leq \Delta H(\text{LiTe}_3), \\
2\mu_{\text{Na}} + \mu_{\text{Te}} &\leq \Delta H(\text{Na}_2\text{Te}), \\
\mu_{\text{Na}} + 3\mu_{\text{Te}} &\leq \Delta H(\text{NaTe}_3), \\
2\mu_{\text{K}} + \mu_{\text{Te}} &\leq \Delta H(\text{K}_2\text{Te}), \\
\mu_{\text{K}} + \mu_{\text{Te}} &\leq \Delta H(\text{KTe}), \\
2\mu_{\text{K}} + 3\mu_{\text{Te}} &\leq \Delta H(\text{K}_2\text{Te}_3), \\
5\mu_{\text{K}} + 3\mu_{\text{Te}} &\leq \Delta H(\text{K}_5\text{Te}_3), \\
\mu_{\text{Be}} + \mu_{\text{Te}} &\leq \Delta H(\text{BeTe}), \\
\mu_{\text{Mg}} + \mu_{\text{Te}} &\leq \Delta H(\text{MgTe}), \\
\mu_{\text{Mg}} + 2\mu_{\text{Te}} &\leq \Delta H(\text{MgTe}_2) \\
\mu_{\text{Ca}} + \mu_{\text{Te}} &\leq \Delta H(\text{CaTe}).
\end{aligned} \tag{8}$$

Here, $\Delta H(\text{Li}_2\text{Te})$, $\Delta H(\text{LiTe}_3)$, $\Delta H(\text{Na}_2\text{Te})$, $\Delta H(\text{NaTe}_3)$, $\Delta H(\text{K}_2\text{Te})$, $\Delta H(\text{KTe})$,

$\Delta H(\text{K}_2\text{Te}_3)$, $\Delta H(\text{K}_5\text{Te}_3)$, $\Delta H(\text{BeTe})$, $\Delta H(\text{MgTe})$, $\Delta H(\text{MgTe}_2)$, and $\Delta H(\text{CaTe})$ are enthalpies of formation for Li_2Te , LiTe_3 , Na_2Te , NaTe_3 , K_2Te , KTe , K_2Te_3 , K_5Te_3 , BeTe , MgTe , and CaTe , respectively. Chemical potentials of Li, Na, K, Be, Mg, and Ca in the growth of MnBi_4Te_7 are capped by the formation of Li_2Te , NaTe_3 , K_2Te_3 , BeTe , MgTe_2 , and CaTe , respectively, at the Te-rich limit and by the formation of Li_2Te , Na_2Te , K_2Te_3 , BeTe , MgTe , and CaTe at the Te-poor limit. The chemical potential of Na in the growth of MnBi_2Te_4 is capped by the formation of NaTe_3 at the Te-rich limit and by the formation of Na_2Te at the Te-poor limit.

The defect density under thermal equilibrium can be calculated by

$$N_D(q, \varepsilon_f) = N_{\text{site}} e^{\frac{-\Delta H(q, \varepsilon_f)}{k_B T}}, \quad (9)$$

where N_{site} is the number of available atomic sites for defect formation, $\Delta H(q, \varepsilon_f)$ is the defect formation energy calculated by Eq. (1), k_B is the Boltzmann constant, and T is temperature. The Fermi level, ε_f , is determined by solving the following equation to satisfy the charge neutrality condition:

$$\sum_{i,j} q_i N_{D_j}(q_i, \varepsilon_f) + n_h - n_e = 0. \quad (10)$$

Here, $N_{D_j}(q_i)$ is the number of the j th defect with a charge state of q_i , calculated using the Eq. 9. The free hole (n_h) and free electron (n_e) densities are calculated by

$$n_h = \int_{-\infty}^{\varepsilon_{VBM}} N_{DOS}(E) [1 - f_e(E, \varepsilon_f, T)] dE \quad (11)$$

and

$$n_e = \int_{\varepsilon_{CBM}}^{\infty} N_{DOS}(E) f_e(E, \varepsilon_f, T) dE, \quad (12)$$

respectively. $N_{DOS}(E)$ is the calculated density of states and $f_e(E, \varepsilon_f)$ is the Fermi-Dirac distribution.

B. Surface energy calculations

We constructed a MnBi_2Te_4 - and a Bi_2Te_3 -terminated symmetric slabs for calculations of surface energies of the two different terminations of the MnBi_4Te_7 (0001) surface. The MnBi_2Te_4 -terminated symmetric slab contains five MnBi_2Te_4 SLs and four Bi_2Te_3 QLs. The Bi_2Te_3 -terminated symmetric slab contains six Bi_2Te_3 QLs and five MnBi_2Te_4 SLs. The vacuum layer included for slab calculations has a thickness of 16 Å. We also tested a much thinner MnBi_2Te_4 -terminated symmetric slab, which contains only three MnBi_2Te_4 SLs and two Bi_2Te_3 QLs. The calculated surface energy difference is only 1.5 meV per surface unit cell. The surface energy is calculated by

$$\Delta H_{surf} = [E_{slab} - \sum_i n_i (\mu_i + \mu_i^{bulk})] / 2A. \quad (13)$$

Here, E_{slab} is the total energy of the slab; μ_i and μ_i^{bulk} are same as those in Eq. (1); A is the surface area. Within the allowed chemical range [the line segment between points A and B in Fig. 2(b)], the following relations always hold: $\mu_{\text{Mn}} + 2\mu_{\text{Bi}} + 4\mu_{\text{Te}} = \Delta H(\text{MnBi}_2\text{Te}_4)$ and $2\mu_{\text{Bi}} + 3\mu_{\text{Te}} = \Delta H(\text{Bi}_2\text{Te}_3)$. Based on these, it can be shown that the calculated surface energy is independent of elemental chemical potentials.

C. Computational details

All calculations are based on density functional theory (DFT)[39,40] implemented in the VASP code.[41] The interaction between ions and electrons is described by the projector augmented wave method[42]. The total energy is calculated using the Perdew-Burke-Eznerhof (PBE) exchange correlation functional[43] and a kinetic energy cutoff

of 270 eV. A U parameter of 4 eV is applied to Mn 3d orbitals[44] and the DFT-D3 vdW functional [45] is used, following several previous DFT studies.[11,12,17] A $3 \times 3 \times 2$ supercell and a $2 \times 2 \times 1$ k-point mesh are used for defect calculations. The c axis is doubled for the AFM calculation. Six SLs are included for MnBi_2Te_4 and MnSb_2Te_4 while two SLs and two QLs are included for MnBi_4Te_7 . Lattice parameters were optimized, and atomic positions were relaxed until the forces are less than 0.02 eV/Å. The optimized lattice constants for MnTe, Bi_2Te_3 , Sb_2Te_3 , MnBi_2Te_4 , and MnBi_4Te_7 are in good agreement with experimental values as shown in Table IV.

Table IV. Calculated lattice parameters compared with experimentally measured values.

		MnTe	Bi_2Te_3	Sb_2Te_3	MnBi_2Te_4	MnBi_4Te_7	MnSb_2Te_4
Cal.	a (Å)	4.158	4.433	4.325	4.365	4.394	4.289
	c (Å)	6.703	30.392	29.973	40.476	23.634	40.301
Exp.	a (Å)	4.148	4.395	4.264	4.3338	4.366	4.2445
	c (Å)	6.711	30.44	30.458	40.931	23.80	40.870
		[46]	[47]	[48]	[24]	[21]	[24]

As mentioned above, a U parameter of 4 eV was used. We tested $U = 3$ eV, 4 eV, and 5 eV for the formation energy calculation of the antisite pair $\text{Bi}_{\text{Mn}}\text{-Mn}_{\text{Bi}}$ in MnBi_4Te_7 , which yields 0.34 eV, 0.33 eV, and 0.32 eV, respectively. This result shows that different choices of the U parameter have a small influence on the defect formation energy.

$U = 4$ eV is appropriate for an insulating Mn compound with local Mn moments, such as MnBi_2Te_4 (calculated magnetic moments: $4.54 \mu_B$ in MnBi_2Te_4 and MnBi_4Te_7

and $4.52 \mu_B$ in MnSb_2Te_4) but should not be applied to Mn metal, which has an itinerant nature. However, for calculations of enthalpies of formation for MnBi_2Te_4 , MnBi_4Te_7 , MnSb_2Te_4 , MnTe , and MnTe_2 , $U = 4$ eV was used for calculating total energies of both insulating Mn compounds and metallic bulk Mn because all parameters used for calculating total energy differences need to be the same. If the error in $\mu_{\text{Mn}}^{\text{bulk}}$, caused by the U parameter, is $\Delta\mu_{\text{Mn}}^{\text{bulk}}$, the enthalpies of formation for MnBi_2Te_4 , MnBi_4Te_7 , MnSb_2Te_4 , MnTe , and MnTe_2 have a systematic error of $-\Delta\mu_{\text{Mn}}^{\text{bulk}}$. However, all these errors do not affect our results for the reasons given below.

For defect formation energy calculations using Eq. 1, only the total chemical potential of Mn, $\mu_{\text{Mn}} + \mu_{\text{Mn}}^{\text{bulk}}$, matters and it is not affected by the error in $\mu_{\text{Mn}}^{\text{bulk}}$ because the error of $-\Delta\mu_{\text{Mn}}^{\text{bulk}}$ in enthalpies of formation of Mn compounds is transferred to μ_{Mn} through Eqs. (2), (4), and (6); consequently, the errors in μ_{Mn} and $\mu_{\text{Mn}}^{\text{bulk}}$ cancel each other.

In fact, the error in $\mu_{\text{Mn}}^{\text{bulk}}$ affects only phase diagrams in Figure 2. Specifically, the error in $\mu_{\text{Mn}}^{\text{bulk}}$ affects $\mu_{\text{Mn}} = 0$ lines in Figure 2 but does not affect phase boundaries between ternary and binary phases due to the error cancelation. Taking MnBi_2Te_4 as an example, the phase boundaries between MnBi_2Te_4 and MnTe and MnTe_2 are determined by

$$\mu_{\text{Te}} \geq -\frac{2}{3}\mu_{\text{Bi}} + \frac{1}{3}[\Delta H(\text{MnBi}_2\text{Te}_4) - \Delta H(\text{MnTe})] \quad (14)$$

and
$$\mu_{\text{Te}} \geq -\mu_{\text{Bi}} + \frac{1}{2}[\Delta H(\text{MnBi}_2\text{Te}_4) - \Delta H(\text{MnTe}_2)], \quad (15)$$

respectively, following Eqs 2-3. The error is canceled when taking the energy difference between two enthalpies of formation.

Next, we estimate how the error in μ_{Mn}^{bulk} affects $\mu_{Mn} = 0$ lines in phase diagrams in Figure 2. Using $MnBi_2Te_4$ as an example again, the $\mu_{Mn} = 0$ line in Figure 2(a) is determined by

$$\mu_{Te} = -\frac{1}{2}\mu_{Bi} + \frac{1}{4}\Delta H(MnBi_2Te_4) \quad (16)$$

(following Eq. 2). Therefore, the error of $-\Delta\mu_{Mn}^{bulk}$ in $\Delta H(MnBi_2Te_4)$ is scaled down by a factor of 4 for the $\mu_{Mn} = 0$ line. We can estimate the error in μ_{Mn}^{bulk} . The calculated $\Delta H(MnTe)$ and $\Delta H(MnTe_2)$ are -1.38 eV and -1.45 eV, respectively. They are lower than their respective measured values of -1.10 eV and -1.30 eV[49] by 0.28 eV and 0.15 eV. Most of the error should come from the artificially high μ_{Mn}^{bulk} . For comparison, the calculated $\Delta H(Bi_2Te_3)$ is -0.97 eV, in good agreement with the experimentally measured value of -1.03 ± 0.1 eV,[50] suggesting that the calculated μ_{Te}^{bulk} is reasonably accurate. If we assign all the errors in calculated $\Delta H(MnTe)$ and $\Delta H(MnTe_2)$ to μ_{Mn}^{bulk} , we obtain an error < 0.28 eV for μ_{Mn}^{bulk} and $\Delta H(MnBi_2Te_4)$. Thus, the error in μ_{Mn}^{bulk} would shift the $\mu_{Mn} = 0$ line up by < 0.07 eV in Fig. 2(a). The corrected $\mu_{Mn} = 0$ line does not intersect the line segment between points A and B. The same analysis can be applied to $MnBi_4Te_7$ and $MnSb_2Te_4$ and show that the error in μ_{Mn}^{bulk} does not affect the chemical potential range (the line segment between points A and B in Fig. 2) used in formation energy calculations. This makes sense because the ternary phases likely have phase boundaries with binary phases but not with elemental phases. Therefore, the error in calculating the total energy of bulk Mn does not affect the results of defect/dopant formation energies in $MnBi_2Te_4$, $MnBi_4Te_7$ and $MnSb_2Te_4$.

ACKNOWLEDGMENTS

The authors are grateful for the stimulating discussion with Yaohua Liu, Matthew Brahlek, and Hu Miao. This work was supported by the U. S. Department of Energy, Office of Science, Basic Energy Sciences, Materials Sciences and Engineering Division.

References

- [1] M. Z. Hasan and C. L. Kane, *Colloquium: Topological insulators*, Reviews of Modern Physics **82**, 3045 (2010).
- [2] X.-L. Qi and S.-C. Zhang, *Topological insulators and superconductors*, Reviews of Modern Physics **83**, 1057 (2011).
- [3] Y. Ando, *Topological Insulator Materials*, Journal of the Physical Society of Japan **82**, 102001 (2013).
- [4] A. Bansil, H. Lin, and T. Das, *Colloquium: Topological band theory*, Reviews of Modern Physics **88**, 021004 (2016).
- [5] C.-Z. Chang *et al.*, *Experimental Observation of the Quantum Anomalous Hall Effect in a Magnetic Topological Insulator*, Science **340**, 167 (2013).
- [6] C.-Z. Chang *et al.*, *High-precision realization of robust quantum anomalous Hall state in a hard ferromagnetic topological insulator*, Nature Materials **14**, 473 (2015).
- [7] R. S. K. Mong, A. M. Essin, and J. E. Moore, *Antiferromagnetic topological insulators*, Physical Review B **81**, 245209 (2010).
- [8] Q. L. He *et al.*, *Chiral Majorana fermion modes in a quantum anomalous Hall insulator–superconductor structure*, Science **357**, 294 (2017).
- [9] M. M. Otrokov *et al.*, *Prediction and observation of an antiferromagnetic topological insulator*, Nature **576**, 416 (2019).
- [10] J. Wu *et al.*, *Natural van der Waals heterostructural single crystals with both magnetic and topological properties*, Science Advances **5**, eaax9989 (2019).
- [11] J. Li, Y. Li, S. Du, Z. Wang, B.-L. Gu, S.-C. Zhang, K. He, W. Duan, and Y. Xu, *Intrinsic magnetic topological insulators in van der Waals layered $\text{MnBi}_{2-x}\text{Te}_4$ -family materials*, Science Advances **5**, eaaw5685 (2019).
- [12] Y. J. Chen *et al.*, *Topological Electronic Structure and Its Temperature Evolution in Antiferromagnetic Topological Insulator MnBi_2Te_4* , Physical Review X **9**, 041040 (2019).
- [13] Y.-J. Hao *et al.*, *Gapless Surface Dirac Cone in Antiferromagnetic Topological Insulator MnBi_2Te_4* , Physical Review X **9**, 041038 (2019).
- [14] R. C. Vidal *et al.*, *Topological Electronic Structure and Intrinsic Magnetization in MnBi_4Te_7 : A Bi_2Te_3 Derivative with a Periodic Mn Sublattice*, Physical Review X **9**, 041065 (2019).
- [15] C. Hu *et al.*, *A van der Waals antiferromagnetic topological insulator with weak interlayer*

- magnetic coupling*, Nature Communications **11**, 97 (2020).
- [16] Y. Deng, Y. Yu, M. Z. Shi, Z. Guo, Z. Xu, J. Wang, X. H. Chen, and Y. Zhang, *Quantum anomalous Hall effect in intrinsic magnetic topological insulator $\text{MnBi}_{2-x}\text{Te}_4$* , Science **367**, 895 (2020).
- [17] C. Liu *et al.*, *Robust axion insulator and Chern insulator phases in a two-dimensional antiferromagnetic topological insulator*, Nature Materials **19**, 522 (2020).
- [18] P. Swatek, Y. Wu, L.-L. Wang, K. Lee, B. Schruck, J. Yan, and A. Kaminski, *Gapless Dirac surface states in the antiferromagnetic topological insulator MnBi_2Te_4* , Physical Review B **101**, 161109 (2020).
- [19] Z. S. Aliev *et al.*, *Novel ternary layered manganese bismuth tellurides of the MnTe-Bi₂Te₃ system: Synthesis and crystal structure*, Journal of Alloys and Compounds **789**, 443 (2019).
- [20] J. Q. Yan *et al.*, *Crystal growth and magnetic structure of MnBi_2Te_4* , Physical Review Materials **3**, 064202 (2019).
- [21] J. Q. Yan, Y. H. Liu, D. S. Parker, Y. Wu, A. A. Aczel, M. Matsuda, M. A. McGuire, and B. C. Sales, *A-type antiferromagnetic order in MnBi_4Te_7 and $\text{MnBi}_6\text{Te}_{10}$ single crystals*, Physical Review Materials **4**, 054202 (2020).
- [22] S. H. Lee *et al.*, *Spin scattering and noncollinear spin structure-induced intrinsic anomalous Hall effect in antiferromagnetic topological insulator MnBi_2Te_4* , Physical Review Research **1**, 012011 (2019).
- [23] A. Zeugner *et al.*, *Chemical Aspects of the Candidate Antiferromagnetic Topological Insulator MnBi_2Te_4* , Chemistry of Materials **31**, 2795 (2019).
- [24] J. Q. Yan, S. Okamoto, M. A. McGuire, A. F. May, R. J. McQueeney, and B. C. Sales, *Evolution of structural, magnetic, and transport properties in $\text{MnBi}_{2-x}\text{Sb}_x\text{Te}_4$* , Physical Review B **100**, 104409 (2019).
- [25] B. Chen *et al.*, *Intrinsic magnetic topological insulator phases in the Sb doped MnBi_2Te_4 bulks and thin flakes*, Nature Communications **10**, 4469 (2019).
- [26] W. Ko *et al.*, *Realizing gapped surface states in magnetic topological insulator $\text{MnBi}_{2-x}\text{Sb}_x\text{Te}_4$* , arXiv:2003.00180.
- [27] Y. S. Hor, A. Richardella, P. Roushan, Y. Xia, J. G. Checkelsky, A. Yazdani, M. Z. Hasan, N. P. Ong, and R. J. Cava, *sp -type Bi_2Se_3 for topological insulator and low-temperature thermoelectric applications*, Physical Review B **79**, 195208 (2009).
- [28] J. G. Checkelsky, Y. S. Hor, M. H. Liu, D. X. Qu, R. J. Cava, and N. P. Ong, *Quantum Interference in Macroscopic Crystals of Nonmetallic Bi_2Se_3* , Physical Review Letters **103**, 246601 (2009).
- [29] Y. Yuan *et al.*, *Electronic States and Magnetic Response of MnBi_2Te_4 by Scanning Tunneling Microscopy and Spectroscopy*, Nano Letters **20**, 3271 (2020).
- [30] D. Souchay *et al.*, *Layered manganese bismuth tellurides with GeBi_4Te_7 - and $\text{GeBi}_6\text{Te}_{10}$ -type structures: towards multifunctional materials*, Journal of Materials Chemistry C **7**, 9939 (2019).
- [31] Y. Hu *et al.*, *Universal gapless Dirac cone and tunable topological states in $(\text{MnBi}_2\text{Te}_4)_m(\text{Bi}_2\text{Te}_3)_n$ heterostructures*, Physical Review B **101**, 161113 (2020).

- [32] Xuefeng Wu *et al.*, *Distinct Topological Surface States on the Two Terminations of MnBi₄Te₇*, arXiv:2002.00320.
- [33] D. West, Y. Y. Sun, H. Wang, J. Bang, and S. B. Zhang, *Native defects in second-generation topological insulators: Effect of spin-orbit interaction on Bi₂Se₃*, Physical Review B **86**, 121201 (2012).
- [34] R. J. Cava, H. Ji, M. K. Fuccillo, Q. D. Gibson, and Y. S. Hor, *Crystal structure and chemistry of topological insulators*, Journal of Materials Chemistry C **1**, 3176 (2013).
- [35] H. Sun *et al.*, *Rational Design Principles of the Quantum Anomalous Hall Effect in Superlattice-like Magnetic Topological Insulators*, Physical Review Letters **123**, 096401 (2019).
- [36] T. Murakami, Y. Nambu, T. Koretsune, G. Xiangyu, T. Yamamoto, C. M. Brown, and H. Kageyama, *Realization of interlayer ferromagnetic interaction in $\text{MnSb}_2\text{T}_2\text{e}_4$ toward the magnetic Weyl semimetal state*, Physical Review B **100**, 195103 (2019).
- [37] R. D. Shannon, *Revised effective ionic radii and systematic studies of interatomic distances in halides and chalcogenides*, Acta Crystallographica Section A **32**, 751 (1976).
- [38] S. Lany and A. Zunger, *Assessment of correction methods for the band-gap problem and for finite-size effects in supercell defect calculations: Case studies for ZnO and GaAs*, Physical Review B **78**, 235104, 235104 (2008).
- [39] P. Hohenberg and W. Kohn, *Inhomogeneous electron gas*, Phys. Rev. **136**, B864 (1964).
- [40] W. Kohn and L. J. Sham, *Self-Consistent Equations Including Exchange and Correlation Effects*, Physical Review **140**, A1133 (1965).
- [41] G. Kresse and J. Furthmüller, *Efficient iterative schemes for *ab initio* total-energy calculations using a plane-wave basis set*, Physical Review B **54**, 11169 (1996).
- [42] G. Kresse and D. Joubert, *From ultrasoft pseudopotentials to the projector augmented-wave method*, Physical Review B **59**, 1758 (1999).
- [43] J. P. Perdew, K. Burke, and M. Ernzerhof, *Generalized gradient approximation made simple*, Physical Review Letters **77**, 3865 (1996).
- [44] S. L. Dudarev, G. A. Botton, S. Y. Savrasov, C. J. Humphreys, and A. P. Sutton, *Electron-energy-loss spectra and the structural stability of nickel oxide: An LSDA+*U* study*, Physical Review B **57**, 1505 (1998).
- [45] S. Grimme, J. Antony, S. Ehrlich, and H. Krieg, *A consistent and accurate *ab initio* parametrization of density functional dispersion correction (DFT-D) for the 94 elements H-Pu*, The Journal of Chemical Physics **132**, 154104 (2010).
- [46] C. Reig, V. Muñoz, C. Gómez, C. Ferrer, and A. Segura, *Growth and characterisation of MnTe crystals*, Journal of Crystal Growth **223**, 349 (2001).
- [47] Y. Feutelais, B. Legendre, N. Rodier, and V. Agafonov, *A study of the phases in the bismuth - tellurium system*, Materials Research Bulletin **28**, 591 (1993).
- [48] T. L. Anderson and H. B. Krause, *Refinement of the Sb₂Te₃ and Sb₂Te₂Se structures and their relationship to nonstoichiometric Sb₂Te₃-*y*Se_y compounds*, Acta Crystallographica Section B **30**, 1307 (1974).
- [49] M. E. Schlesinger, *The Mn-Te (manganese-tellurium) system*, Journal of Phase Equilibria **19**, 591 (1998).
- [50] V. R. Sidorko, L. V. Goncharuk, and R. V. Antonenko, *Thermodynamic properties of bismuth sesquiselenide and sesquitelluride and their solid solutions*, Powder Metallurgy and Metal

Ceramics **47**, 234 (2008).